



HAL
open science

M Subdwarf Research. III. Spectroscopic Diagnostics for Breaking Parameter Degeneracy

Shuo Zhang, Hua-Wei Zhang, Georges Comte, Derek Homeier, Rui Wang,
Neda Hejazi, Yin-Bi Li, A. -Li Luo

► **To cite this version:**

Shuo Zhang, Hua-Wei Zhang, Georges Comte, Derek Homeier, Rui Wang, et al.. M Subdwarf Research. III. Spectroscopic Diagnostics for Breaking Parameter Degeneracy. *The Astrophysical Journal*, 2023, 942, 10.3847/1538-4357/aca28d . insu-04479122

HAL Id: insu-04479122

<https://insu.hal.science/insu-04479122>

Submitted on 1 Mar 2024

HAL is a multi-disciplinary open access archive for the deposit and dissemination of scientific research documents, whether they are published or not. The documents may come from teaching and research institutions in France or abroad, or from public or private research centers.

L'archive ouverte pluridisciplinaire **HAL**, est destinée au dépôt et à la diffusion de documents scientifiques de niveau recherche, publiés ou non, émanant des établissements d'enseignement et de recherche français ou étrangers, des laboratoires publics ou privés.



Distributed under a Creative Commons Attribution 4.0 International License



M Subdwarf Research. III. Spectroscopic Diagnostics for Breaking Parameter Degeneracy

Shuo Zhang (张硕)^{1,2}, Hua-Wei Zhang (张华伟)^{1,2}, Georges Comte³, Derek Homeier⁴, Rui Wang (王瑞)⁵, Neda Hejazi^{6,7}, Yin-Bi Li (李荫碧)⁵, and A-Li Luo (罗阿理)^{5,8}

¹ Department of Astronomy, School of Physics, Peking University, Beijing 100871, People's Republic of China; szhang0808@pku.edu.cn

² Kavli Institute of Astronomy and Astrophysics, Peking University, Beijing 100871, People's Republic of China; zhanghw@pku.edu.cn

³ Aix-Marseille Univ, CNRS, CNES, LAM, Laboratoire d'Astrophysique de Marseille, Marseille, France

⁴ Zentrum für Astronomie der Universität Heidelberg, Landessternwarte, Königstuhl 12, D-69117 Heidelberg, Germany

⁵ CAS Key Laboratory of Optical Astronomy, National Astronomical Observatories, Beijing 100101, People's Republic of China

⁶ Department of Physics and Astronomy, University of Kansas, Lawrence, KS 66045, USA

⁷ Department of Physics and Astronomy, Georgia State University, Atlanta, GA 30303, USA

⁸ University of Chinese Academy of Sciences, Beijing 100049, People's Republic of China

Received 2022 May 12; revised 2022 November 10; accepted 2022 November 10; published 2023 January 6

Abstract

To understand the parameter degeneracy of M subdwarf spectra at low resolution, we assemble a large number of spectral features in the wavelength range 0.6–2.5 μm with band strength quantified by narrowband indices. Based on the index trends of BT-Settl model sequences, we illustrate how the main atmospheric parameters (T_{eff} , $\log g$, $[M/H]$, and $[\alpha/\text{Fe}]$) affect each spectral feature differently. Furthermore, we propose a four-step process to determine the four parameters sequentially, which extends the basic idea proposed by Jao et al. Each step contains several spectral features that break the degeneracy effect when determining a specific stellar parameter. Finally, the feasibility of each spectroscopic diagnostic with different spectral quality is investigated. The result is resolution-independent down to $R \sim 200$.

Unified Astronomy Thesaurus concepts: M stars (985); M subdwarf stars (986); Stellar atmospheres (1584); Stellar effective temperatures (1597); Stellar abundances (1577)

1. Introduction

Low-mass stars ($M < 0.8 M_{\odot}$) are the main stellar component of the Milky Way. They account for 70% of the total number of stars and occupy 40% of the total stellar mass of the galaxy (Reid & Gizis 1997; Chabrier 2003; Henry et al. 2006; Bochanski et al. 2010; Winters et al. 2015; Reylé et al. 2021). The M-type low-mass stars at the end of the main sequence in the H-R diagram contain a variety of exciting stellar components, including the most dominant stellar members of the Galactic disk, M dwarfs; the rare Population II stars, M subdwarfs; and some of the substellar objects, degenerate brown dwarfs. The M dwarfs have contributed significantly to studies of the initial mass function (e.g., Conroy & van Dokkum 2012; McConnell et al. 2016), as well as the mass-to-light ratio of nearby galaxies (Muirhead et al. 2015; Spiniello et al. 2015), and they are also popular candidate hosts with Earth-sized planets orbiting within the habitable zone (e.g., Dressing & Charbonneau 2013). Their metal-poor counterparts, subdwarfs that associated kinematically with the thick disk and halo (e.g., Bochanski et al. 2013), are of importance as the probes of the old galactic populations. Besides, young brown dwarfs with mass just below the hydrogen-burning minimum mass are sometimes classified as spectral types M7–M9, mixed with the ultracool dwarfs/subdwarfs with mass $\leq 0.1 M_{\odot}$ (Dupuy & Liu 2017; Zhang 2019).

As the members of old Galactic populations (see, e.g., Mould 1976a; Lépine et al. 2007; Bochanski et al. 2013;

Kesseli et al. 2019), M subdwarfs are, on average, much older than the M dwarfs with solar metallicity. The surface chemical compositions of these unevolved main-sequence stars are not changed by various enrichment processes and retain the chemical footprint of the gas from which they formed (e.g., Hejazi et al. 2022). This makes them fossil record and golden tracers of the earliest phases of the assembly of the Milky Way.

Measuring basic atmospheric parameters is challenging for M-type low-mass stars because the spectra of these stars with cool atmospheres (2500–4000 K) are dominated by molecular absorption bands hiding or blending with the atomic lines, which leaves no windows onto the continuum (Allard 1990; Rajpurohit et al. 2014; Passegger et al. 2016). For M dwarfs, stellar properties have been studied relatively thoroughly and generally determined separately. For example, the effective temperature (T_{eff}) of M dwarfs can be derived from the empirical T_{eff} -color relationship (e.g., Mann et al. 2015, 2019) or T_{eff} -index relationship (Rojas-Ayala et al. 2012), while metallicity ($[\text{Fe}/\text{H}]$) can be estimated via relations of near-infrared (NIR) K -band magnitudes alongside optical photometry (Bonfils et al. 2005; Neves et al. 2012) and calibrated by binaries containing an FGK-type companion (e.g., Bonfils et al. 2005; Mann et al. 2013a; Rains et al. 2021). Interferometric diameters and dynamical masses have been utilized to calibrate mass and radius relations (e.g., Delfosse et al. 2000; Benedict et al. 2016). In some works, comparing synthetic spectra over broad spectral ranges (Rajpurohit et al. 2013; Gaidos & Mann 2014; Du et al. 2021) or a series of selected feature bands (Passegger et al. 2016, 2018) to determine several parameters at once is opted for.

However, for metal-poor subdwarfs, the situation is more complicated because metallicity severely affects the energy distribution in low-mass stars (Delfosse et al. 2000). Due to the



Original content from this work may be used under the terms of the [Creative Commons Attribution 4.0 licence](https://creativecommons.org/licenses/by/4.0/). Any further distribution of this work must maintain attribution to the author(s) and the title of the work, journal citation and DOI.

scarcity in the solar neighborhood, it is difficult to obtain enough binaries containing metal-poor FGK star companions that can cover the entire metal abundance range. The low intrinsic brightness of subdwarfs further makes it difficult to acquire adequate high-resolution spectra covering the extended parameter grid, resulting in a poor constraint to the theoretical models. The near one-to-one mass–radius relation for the low-mass dwarfs (Benedict et al. 2016) is no longer effective because metal deficiency modifies the equilibrium configuration of the atmospheres of subdwarfs, leading to smaller radii at the same temperature (Kesseli et al. 2019). In addition, it is hard to obtain high-quality spectra in the optical because their spectral energy distributions peak at 0.8–1 μm , while the infrared spectra are seriously contaminated by telluric absorption. To date, comparing observed spectra with grids of synthetic spectra using χ^2 minimization in multidimensional parameter space is still the preferred method (Rajpurohit et al. 2013, 2014, 2016; Lodieu et al. 2019; Hejazi et al. 2020; Zhang et al. 2021; Hejazi et al. 2022).

When estimating parameters through a synthetic fitting process, parameter degeneracy usually occurs as a problem, because the strength of the molecular features is a function of both T_{eff} and metallicity (Rains et al. 2021). For the metal-poor objects, the enhancement of α -elements (Ne, Mg, Si, S, Ar, Ca, and Ti) also impacts the spectral shape over a wide range of wavelength regions (Hejazi et al. 2022). According to Hejazi et al. (2022), who conducted a study on pairwise degeneracy of T_{eff} , $\log g$, $[\text{M}/\text{H}]$, and $[\alpha/\text{Fe}]$, the effects on the spectrum from increasing metal abundance within a certain range can be counteracted by the effect of an increase in T_{eff} or surface gravity or a decrease in $[\alpha/\text{Fe}]$. Therefore, uncertainty is introduced in the fitting process due to a series of synthetic spectra with similar spectral morphology but different parameter combinations.

In this work, we aim to conduct an extended exploration of spectral degeneracy for M subdwarfs in the optical and NIR when more than two parameters are involved. The paper is organized as follows. Section 2 explores parameter degeneracy at various feature bands via spectral indices of model sequences. To break degeneracy, a four-step process for sequentially estimating T_{eff} , $[\text{M}/\text{H}]$, $[\alpha/\text{Fe}]$, and $\log g$ is proposed. Section 3 discusses the effects of different spectral quality and resolution. Finally, we summarize our study in Section 4.

2. Spectroscopic Diagnostics Determination

In the optical and NIR spectra of low-mass stars, the most significant opacity sources are metal oxide species such as TiO and CO; hydrides such as SiH, CaH, FeH, and CrH; hydroxides such as CaOH; and water vapor (Rajpurohit et al. 2013, 2016). The molecular absorption features consist of thousands of individual lines affecting both the detailed structure of the spectrum and the global structure of the atmosphere (Valenti et al. 1998) blending to overlapped absorption bands in the low-resolution spectra.

Narrowband indices were usually designed to estimate the strengths of individual spectral features, which measure the flux ratios between the feature bands and sidebands (“pseudocontinuum”). Utilizing narrowband indices with a detailed understanding of the corresponding spectral features, one can design effective schemes in estimating parameters. For example, Mould (1976b) predicted that TiO absorption decreases in

strength with decreasing $[\text{M}/\text{H}]$, but the hydride bands are largely unaffected; this qualitative result was quantified by Gizis (1997), who used several indices (CaH1, CaH2, CaH3, TiO5) to measure the strengths of CaH and TiO bands and developed the first subdwarf classification system. It is worth noting that a parameter $\zeta_{\text{TiO}/\text{CaH}}$ was then introduced by Lépine et al. (2007) to quantify the weakening of the TiO band strength. Its relationships with $[\text{Fe}/\text{H}]$ and $[\text{M}/\text{H}] + [\alpha/\text{Fe}]$ were determined by Woolf et al. (2009) and Hejazi et al. (2020), respectively.

The precondition of breaking degeneracy is a detailed understanding of the complicated dependence of more spectral features on atmospheric parameters. In this section, we propose a solution to parameter measurement following and extending the basic idea of Jao et al. (2008), who proposed a three-step method to break the degeneracy. The parameter degeneracy effect is further and deeply explored based on multiple spectral indices. Note that the analysis of the index trend is based on the synthetic spectra and hence influenced by the incompleteness of the models. Nevertheless, these trends can still play a theoretical guiding role.

2.1. PHOENIX BT-Settl Model Grid

In the present study, we have used the latest BT-Settl CIFIST stellar atmosphere models (Allard et al. 2012, 2013, 2014; Baraffe et al. 2015) also used in Hejazi et al. (2020, 2022). Compared with the classical grids available from the CIFIST project,⁹ this newly calculated model grid¹⁰ also varies over a range of α -element enhancements, $[\alpha/\text{Fe}]$, as a subgrid. These atmosphere models are computed with the PHOENIX multi-purpose atmosphere code version 15.5 (Hauschildt et al. 1997; Allard et al. 2001), including specialized models for the coolest (below 3000 K) stellar and brown dwarf atmospheres using the Settl model of cloud formation, as well as the radiation hydrodynamic simulations of M-L-T dwarf atmospheres (Freytag et al. 2010, 2012).

Since the release of the BT-Settl model atmospheres, the precalculated synthetic spectra have been widely used in numerous spectroscopic analyses with observations and measure the atmospheric parameters (e.g., Mann et al. 2013b; Rajpurohit et al. 2013, 2014; Mann et al. 2015; Rajpurohit et al. 2016; Veyette et al. 2017; Zhang et al. 2017a, 2017b; Rajpurohit et al. 2018a, 2018b; Zhang 2019; Hejazi et al. 2020; Dieterich et al. 2021; Zhang et al. 2021; Hejazi et al. 2022). The results show that BT-Settl models are successful in reproducing the overall optical-NIR spectral profile of M and L subdwarfs, particularly at $[\text{Fe}/\text{H}] \leq -1.0$ dex (Zhang et al. 2017b), and most of the molecular and atomic features can be well fitted with the observations (Rajpurohit et al. 2014).

In this work, we use the synthetic spectra instead of the observed spectra for the subsequent investigation because the parameter space of the model grid is uniform and extended to metallicities as low as $[\text{M}/\text{H}] = -3.0$ dex, required for our analysis. The variation of a spectrum solely caused by changing atmospheric parameters can be explored. The parameter space is shown in Table 1, and the precalculated synthetic spectra have been convolved down to $R \sim 2000$ in the following analyses. At this resolution, the uncertainty introduced by the imperfection of the models can be referred

⁹ <https://phoenix.ens-lyon.fr/Grids/BT-Settl/CIFIST2011/>

¹⁰ These models have not yet been made publicly available by the team.

Table 1
Parameter Space of the Model Grid Used in This Work

| Variable | Range | Step Size |
|------------------|---|-----------|
| T_{eff} | 2500–4000 K | 100 K |
| $\log g$ | 4.5–5.5 dex | 0.5 dex |
| [M/H] | –3.0 to +0.5 dex | 0.5 dex |
| [α /Fe] | –0.2 to +0.2 dex for [M/H] \geq 0.0 0.0 to +0.4 dex for [M/H] = –0.5 +0.2 to +0.6 dex for [M/H] \leq –1.0 | 0.2 dex |

to the quantitative results from Hejazi et al. (2020, 2022), in which the authors measured that the maximum discrepancies between observations and best-fit synthetic spectra are 5%–15%, depending on the temperature range and wave bands.

2.2. Exploration of Temperature Indicators

To serve as a qualified temperature indicator, a spectral feature with the following characteristics is expected: varying regularly and monotonically with temperature and almost independent of the effects of any other atmospheric parameter. In the following, we examine and discuss a class of indices with such properties—pseudocontinuum colors—in great detail.

2.2.1. Pseudocontinuum Colors

In general, the overall optical-to-NIR spectrum is largely depressed by molecular opacity in stars as cool as M subdwarfs; as a result, the true stellar continuum cannot be identified. However, at a few wavelength points, the molecules are a little more transparent, and one can see deeper into the photosphere, forming a pseudocontinuum (Kirkpatrick et al. 1991; Martin et al. 1996). Therefore, “pseudocontinuum colors” have been defined to estimate the slope of the pseudocontinuum wavelength regions (Hamilton & Stauffer 1993; Martin et al. 1996; Martin et al. 1999; Hawley et al. 2002; Lépine et al. 2003; Covey et al. 2007; Yi et al. 2014).

We have collected 16 such “colors” from the literature and examined the dependence of each of them on atmospheric parameters. The pseudocontinuum colors are defined as

$$\text{Color} = \frac{\text{Average Flux Density (Numerator)}}{\text{Average Flux Density (Denominator)}} \quad (1)$$

where Numerator and Denominator are spectral regions within the reference wavelengths listed in Table A1 in the Appendix. The results show that some of these colors are almost insensitive to metallicity and surface gravity, which makes them strong competitors for the temperature calibrators of subdwarfs.

To measure the variable value range of each color at different temperatures as closely as possible to real conditions, we select the entire model grid from 2500 to 4000 K with all available gravity, metallicity, and alpha-enhancement values listed in Table 1 and measure the pseudocontinuum colors for each of these synthetic spectra. We then group the synthetic spectra by temperature and calculate the mean and standard deviation of all colors associated with the spectra in each group, as compared in Figure 1.

From the colors shown in the main panel of Figure 1, we find three colors with quite a small dispersion for each temperature group and show them in the inset of Figure 1. The trend of the commonly used spectral typing indicator, CaH2+CaH3 (Lépine et al. 2007), is also demonstrated in the inset for comparison. Due to the exclusive dependence of the three pseudocontinuum colors, PC4, PC5, and Color-H02, on the temperature when $T_{\text{eff}} \geq 3000$ K, we choose them to be the temperature indicators.

2.2.2. Two Additional Pseudocontinuum Colors

Considering that all three selected colors have a reference band beyond 9000 Å where the observed spectra are dominated by strong telluric absorptions, we have further explored alternatives at bluer wavelengths. For this purpose, we have defined five bands listed in Table 2 pertaining to pseudocontinuum points within 6000–9000 Å that are less depressed by molecular opacity. Computed from every two bands, a pseudocontinuum color can measure the slope of the pseudocontinuum within the corresponding wavelength ranges. The upper panel of Figure 2 shows these bands on a synthetic spectrum as an example.

After the exploration of all possible colors formed by the above five bands, we find that the pseudocontinuum slopes between the last three bands are mainly dependent on temperature, rather than other parameters. The dispersions of the pseudocolors C88-81 and C81-75 are shown in the bottom panels of Figure 2. Pseudocolor C88-81 has a regular dependence on the temperature, with a small and constant dispersion down to ~ 3000 K. Note that the relatively small color range makes it a temperature indicator that would be subject to measurement uncertainties. On the other hand, C81-75 has a larger dynamic range, although its increasing dispersion toward lower temperatures may limit its applicability. For quantitative comparison, Table 3 lists the typical dispersion values for each pseudocontinuum color at different temperatures.

Caution should be taken when using these colors at low temperatures ($T_{\text{eff}} < 3000$ K), where the color ranges related to the temperature groups rapidly increase. As the temperature decreases below 3000 K, the increasing effect of molecular opacity and cloud formation on stellar atmospheres makes the modeling more complex and difficult (Allard et al. 2012). The optical spectra no longer change sensitively with T_{eff} due to dust formation (Rajpurohit et al. 2013). In addition, the pseudocontinuum colors also begin to be sensitive to other parameters. If they are still being used as temperature indicators, a much larger uncertainty would thus be introduced.

In the following, we conduct a more extensive investigation of NIR spectral features redder than 1 μm as a supplement and recommend some of them as temperature tracers for the ultracool subdwarfs.

2.2.3. NIR Temperature Indicators

Spectroscopy at NIR wavelengths is involved with a wide range of available atomic and molecular absorption features, especially water vapor absorption bands. Various studies of late-type M dwarfs and brown dwarfs have defined spectral indices to characterize the molecular bands at different wavelengths, such as H₂O, CH₄, CO, and FeH.

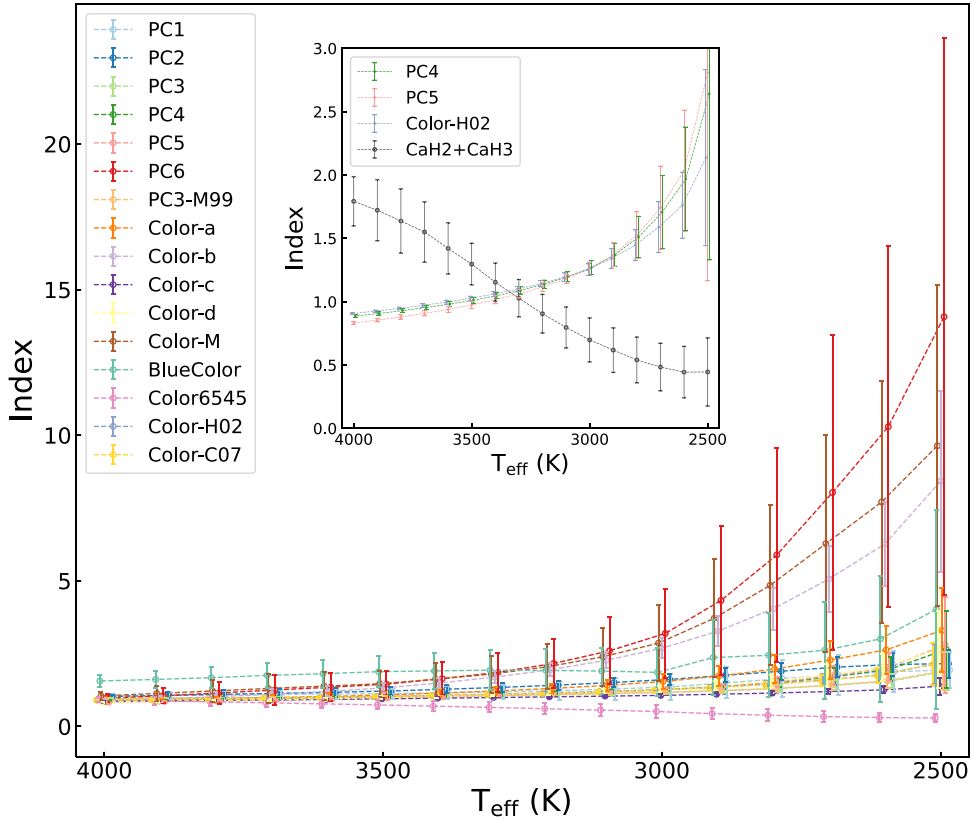


Figure 1. Main panel: value dispersion of 16 pseudocontinuum colors defined in the literature. The entire model grid from 2500 to 4000 K with all available gravity, metallicity, and alpha-enhancement values is used to calculate. The synthetic spectra are grouped by temperature, and the mean and standard deviation (shown as the error bars) of each group are calculated for each color. In the inset, the three selected pseudocontinuum colors are shown compared with the composite index CaH2+CaH3. Their typical dispersion values for different temperatures are listed in Table 3.

Table 2
Pseudocontinuum Bands Defined in This Work

| Band | Name | λ_{begin} (Å) | λ_{end} (Å) |
|------|------|------------------------------|----------------------------|
| 1 | C66 | 6590 | 6645 |
| 2 | C70 | 7042 | 7049 |
| 3 | C75 | 7545 | 7580 |
| 4 | C81 | 8145 | 8165 |
| 5 | C88 | 8833 | 8855 |

Note. The colors are named “CYY-XX,” where YY and XX each represent a reference band, and calculated following Equation (1), e.g., C81-66 = $\frac{\text{Average Flux within Band 4}}{\text{Average Flux within Band 1}}$.

We inspect the following 75 indices from the literature characterizing feature bands redder than $1 \mu\text{m}$: K1, K2 (Tokunaga & Kobayashi 1999), Q (Cushing et al. 2000), water index (McLean et al. 2000), H₂O^A, H₂O^B, H₂O^C, H₂O^D (Reid et al. 2001), sHJ, sKJ, sH₂O^J, sH₂O^{H1}, sH₂O^{H2}, sH₂O^K (Testi et al. 2001), H₂O-A, H₂O-B, H₂O-C, CH₄-A, CH₄-B, CH₄-C, H/J, K/J, K/H, CO, 2.11/2.07, K shape (Burgasser et al. 2002), $1.0 \mu\text{m}$, H₂O-1.2, H₂O-1.5, CH₄-1.6, H₂O-2.0, CH₄-2.2 (Geballe et al. 2002), H₂OA, H₂OB, H₂OC, H₂OD, CH₄A, CH₄B, CO, J-FeH, z-FeH (McLean et al. 2003), H₂O-1, H₂O-2, FeH (Slesnick et al. 2004), z-VO (Cushing et al. 2005), H₂O-J, H₂O-H, H₂O-K, CH₄-J, CH₄-H, CH₄-K, K/J (Burgasser et al. 2006), H₂O, Na (Allers et al. 2007), WH, WK, QH, QK (Weights et al. 2009), H-dip (Burgasser et al. 2010), H₂O-H, H₂O-K (Covey et al. 2010), H₂O-K2 (Rojas-Ayala et al. 2012), HPI (Scholz et al. 2012) FeH_z, VO_z, FeH_JK I_J, H-cont

(Allers & Liu 2013), W₀, W_D, W₁, W₂ (Zhang et al. 2018), TLI-J, TLI-K, TLI-g (Almendros-Abad et al. 2022).

After evaluating the dependence on atmospheric parameters of all indices, we recommend using three of them as temperature indicators: H₂O-1, H₂O-B, and TLI-K. The indices can be calculated as

$$R_{\text{ind}} = \frac{F_{\text{W}}}{F_{\text{cont}}}, \quad (2)$$

where the pseudocontinuum (F_{cont}) region and the feature (F_{W}) wavelength limits are listed in Table A2 in the Appendix.

As shown in Figure 3, the index H₂O-1 has a regular temperature dependence at 2500–3500 K. Note that it also has a modest metal abundance dependence that increases slightly with decreasing temperature. Therefore, two other indices, i.e., H₂O-B and TLI-K, are supplemented because they present more reliable temperature indicators for solar-abundant to moderately metal-poor stars (dM/sdM).

In total, eight spectral features consisting of five pseudocontinuum colors (three from the literature and two defined in this work) and three spectral indices (redder than $1 \mu\text{m}$) are provided as qualified temperature indicators.

2.3. Spectral Features for Estimating $[M/H]$ and $[\alpha/Fe]$

In the classification criteria of Jao et al. (2008), TiO5 band strength was used to determine the metallicity level (see Section 5 in their paper) because the authors claimed that this band strength is highly sensitive to metal abundance variation while being almost unaffected by surface gravity. In the left

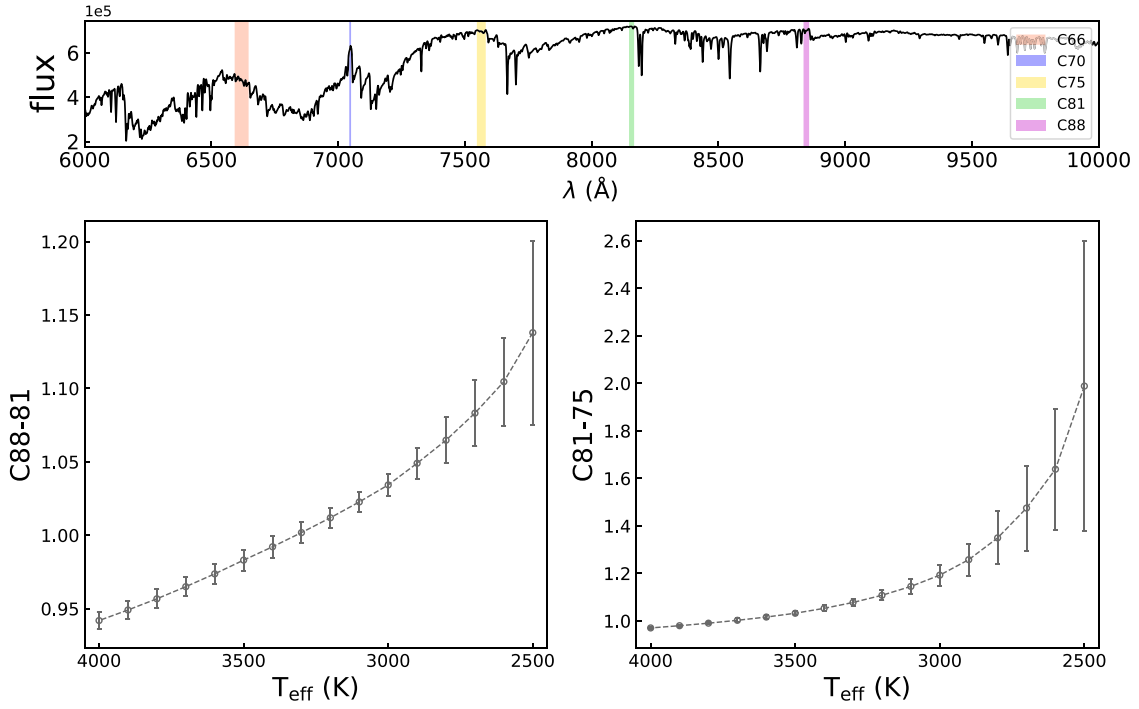


Figure 2. Upper panel: bands listed in Table 2 shown on a synthetic spectrum of 3500 K. Bottom panels: two new pseudocontinuum colors defined in Section 2.2.2 that are almost sensitive only to the effective temperature at $T_{\text{eff}} \geq 3000$ K. Table 3 lists their typical dispersion values for different temperatures.

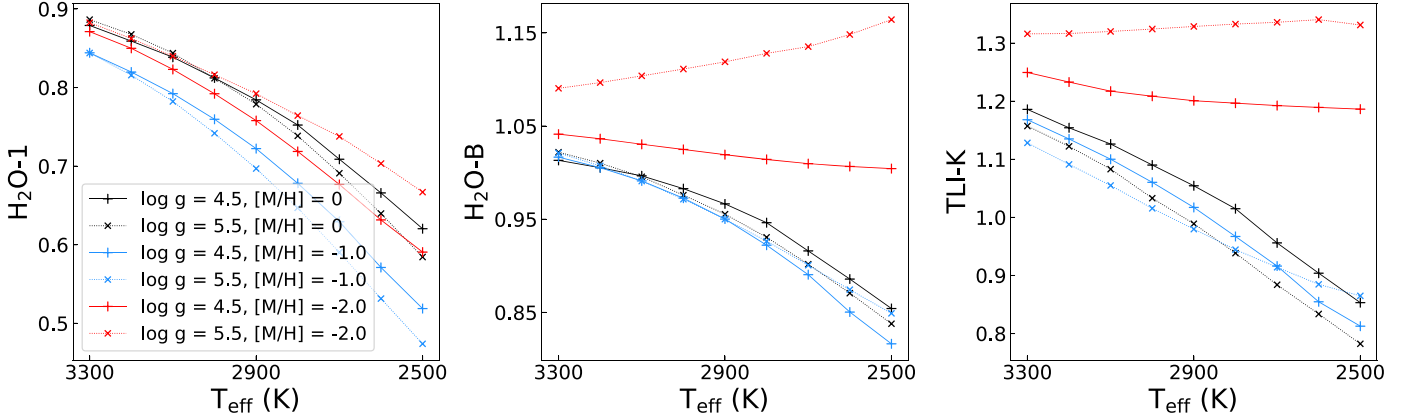


Figure 3. Infrared indices as temperature indicators for ultracool dwarfs. Models are plotted with the following colors: black refers to solar metallicity with $[\alpha/\text{Fe}] = 0.0$, blue refers to metallicity of -1.0 dex with $[\alpha/\text{Fe}] = 0.4$ dex, and red refers to -2.0 dex with 0.4 dex; solid lines are for $\log g = 4.5$ models and dotted lines for $\log g = 5.5$ models.

panel of Figure 4, we explore the complex dependence of TiO5 on atmospheric parameters based on model sequences with different metal abundances and surface gravity. Some other indices that have similar behavior, e.g., TiO2, TiO3, TiO4, and CaOH, are also shown in the right panels of Figure 4.

Two shortcomings limit the reliability of these indices as an indicator of metal abundance, as illustrated in Figure 4. First, at high temperatures (~ 3300 – 4000 K), the index values for the solar metallicity to moderate metal-poor models are very sensitive to surface gravity. As shown in the left panel, increasing surface gravity and decreasing metal abundance have similar effects on TiO5 index values. Second, when the temperature drops below ~ 3300 K, the index for the models of solar abundance to moderate metal deficiency ($[\text{M}/\text{H}] = -1.0$ dex) loses its sensitivity to metal abundance, leaving the extremely metal-poor models as the only ones that can be

distinguished. In addition, when the temperature drops below ~ 2700 K, the index completely loses its ability to determine metal abundance levels due to the disappearance of the TiO molecular bands.

Besides, TiO is highly sensitive to α -abundance, which makes it an indicator of $[\alpha/\text{H}]$ rather than the overall metallicity $[\text{M}/\text{H}]$. Although the values of $[\alpha/\text{Fe}]$ and $[\text{M}/\text{H}]$ generally maintain a correlation, the α -abundances still differ for every single star and need to be determined individually. For example, the widely used model grids, such as the classical model grid from the CIFIST project or the MARCS model grid (Gustafsson et al. 2008), assume $[\alpha/\text{Fe}]$ as a function of $[\text{M}/\text{H}]$ based on the rough estimate of $[\alpha/\text{Fe}]$ for the thin and thick disk. For this reason, $[\alpha/\text{Fe}]$ has been considered as a fixed parameter in many studies. However, large spectroscopic surveys like the Apache Point Observatory Galaxy Evolution

Table 3
Typical Dispersion for Different Effective Temperatures

| Index | 4000 | 3900 | 3800 | 3700 | 3600 | 3500 | 3400 | T_{eff} (K) | 3300 | 3200 | 3100 | 3000 | 2900 | 2800 | 2700 | 2600 | 2500 |
|-----------|--------|--------|--------|--------|--------|--------|--------|----------------------|--------|--------|--------|--------|--------|--------|--------|--------|------|
| CaH2+CaH3 | 0.1947 | 0.2412 | 0.2536 | 0.2383 | 0.2019 | 0.1640 | 0.1507 | 0.1470 | 0.1524 | 0.1618 | 0.1739 | 0.1759 | 0.1806 | 0.1878 | 0.2033 | 0.2690 | |
| PC4 | 0.0120 | 0.0125 | 0.0142 | 0.0181 | 0.0215 | 0.0233 | 0.0265 | 0.0291 | 0.0320 | 0.0394 | 0.0547 | 0.0901 | 0.1641 | 0.2892 | 0.4100 | 1.3107 | |
| PC5 | 0.0117 | 0.0135 | 0.0162 | 0.0199 | 0.0242 | 0.0282 | 0.0313 | 0.0327 | 0.0334 | 0.0373 | 0.0522 | 0.0924 | 0.1840 | 0.3280 | 0.4790 | 1.6421 | |
| Color-H02 | 0.0066 | 0.0079 | 0.0099 | 0.0129 | 0.0151 | 0.0168 | 0.0194 | 0.0219 | 0.0255 | 0.0334 | 0.0462 | 0.0767 | 0.1199 | 0.1996 | 0.2608 | 0.6954 | |
| C81-75 | 0.0047 | 0.0042 | 0.0050 | 0.0082 | 0.0091 | 0.0091 | 0.0121 | 0.0160 | 0.0216 | 0.0306 | 0.0437 | 0.0668 | 0.1116 | 0.1786 | 0.2551 | 0.6115 | |
| C88-81 | 0.0058 | 0.0062 | 0.0064 | 0.0066 | 0.0068 | 0.0072 | 0.0073 | 0.0071 | 0.0067 | 0.0067 | 0.0075 | 0.0106 | 0.0155 | 0.0226 | 0.0300 | 0.0626 | |

Note. The typical dispersion values for the five pseudocontinuum colors at different effective temperatures. The classical compound index CaH2+CaH3 is presented for comparison.

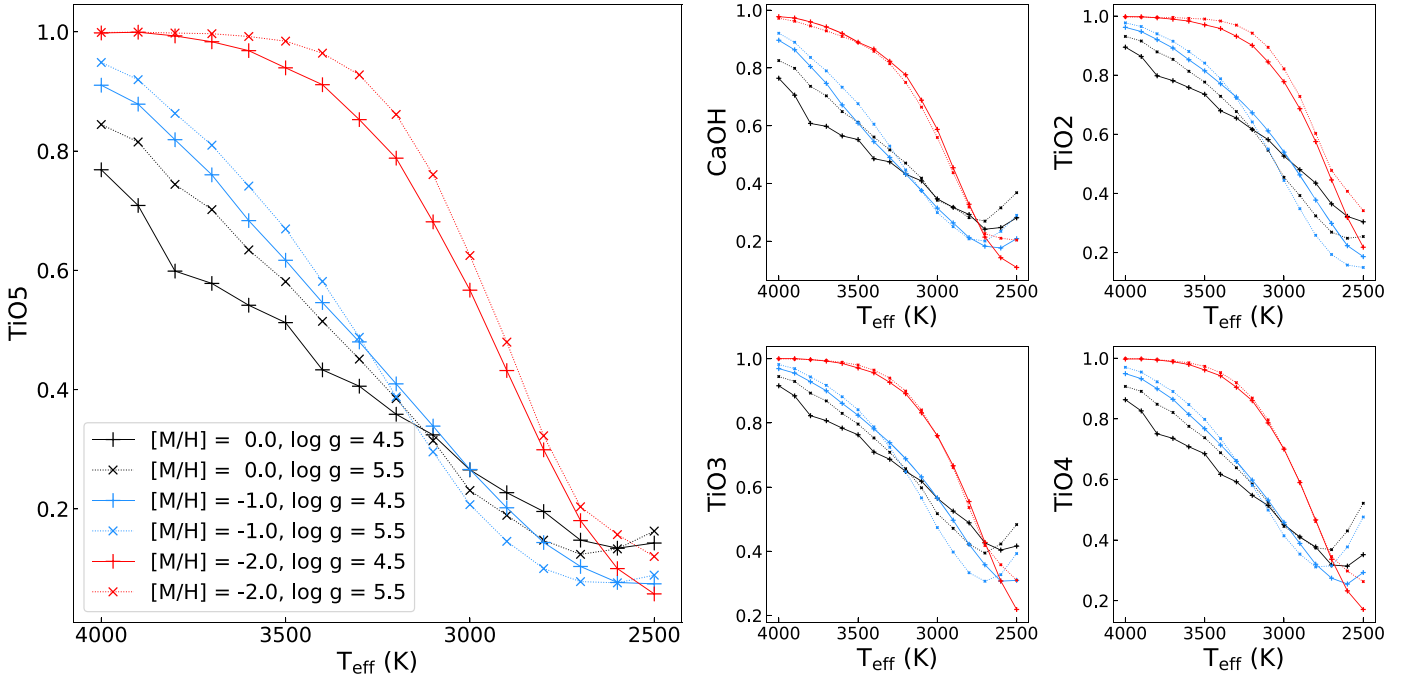


Figure 4. The TiO bands represented by the indices of TiO2, TiO3, TiO4, and TiO5 vs. the effective temperature. In addition, the CaOH index behaving similarly to the TiO indices is also shown. Models are plotted with the same colors as in the above figure.

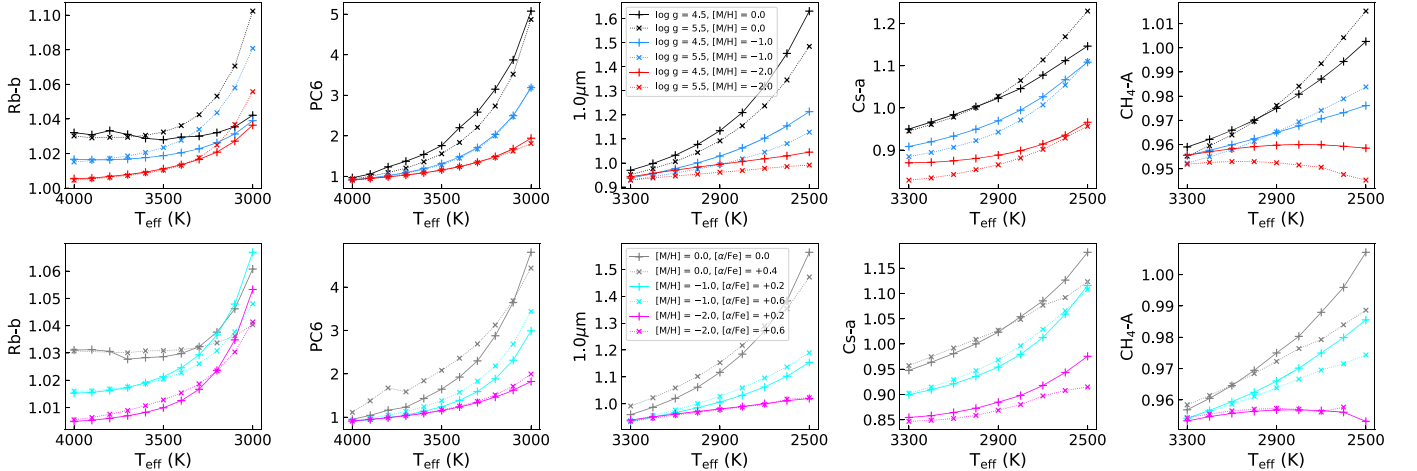


Figure 5. Spectral indices with low sensitivity to both surface gravity and α -enhancement. The upper panels show the model sequences with the same colors as in the figures above. The bottom panels show the same indices but of model sequences with $\log g$ fixed at 5.0 and varied $[\alpha/\text{Fe}]$ values.

Experiment (APOGEE; Majewski et al. 2010; Hayden et al. 2015) and Galactic Archaeology with HERMES (GALAH; Buder et al. 2021) have shown significant scatters around the tight relations assumed in the model grids.

The α -element abundance affects the spectral shape in roughly the same way with $[\text{M}/\text{H}]$. An increase in $[\text{M}/\text{H}]$ may be counteracted by a decrease in $[\alpha/\text{Fe}]$, and vice versa (Hejazi et al. 2022). Therefore, to infer a more accurate $[\text{M}/\text{H}]$, one needs spectral features that are sensitive to neither surface gravity nor α -enhancement but to changes in $[\text{M}/\text{H}]$ from solar abundance to extreme metal deficiency (provided that the temperature has already been measured).

To search for spectral features with such characteristics, we also explore more spectral features with reference wave bands within $1\mu\text{m}$ defined in the typical studies of M dwarfs/subdwarfs in addition to the NIR indices listed in Section 2.2.3,

including CaH 6975, Ti_i 7385, Na_i 8183,8195 (Kirkpatrick et al. 1991), CaOH, CaH1, CaH2, CaH3, TiO1, TiO2, TiO3, TiO4, TiO5 (Reid et al. 1995), VO ratio (Kirkpatrick et al. 1995), TiO1, TiO2, VO1, VO2, CrH1, CrH2, FeH1, FeH2, H₂ O1 (Martín et al. 1999), VO-a, VO-b, Rb-b, Cs-a, CrH-a (Kirkpatrick et al. 1999), TiO 8440, VO 7434, VO 7912, Na 8190 (Hawley et al. 2002), TiO6, VO2 (Lépine et al. 2003), Ca_i 4227, G band, Fe_i 4383, Fe_i 4405, Mg_i 5172, Na D, Mg_i 5172, TiO B, VO 7912, Na_g 8189, Fe_i 8689, Ca_{ii} 8498, Ca_{ii} 8542, Ca_{ii} 8662 (Covey et al. 2007), CaH, and TiO 8250 (Yi et al. 2014).

As a result, we select some of these indices for subsequent analysis and list their reference bands in Table A2 in the Appendix. Five spectral indices exhibiting the expected characteristic within different temperature scopes are shown in Figure 5. In the temperature range of 3000–4000 K, Rb and PC6 show very little sensitivity to both gravity and

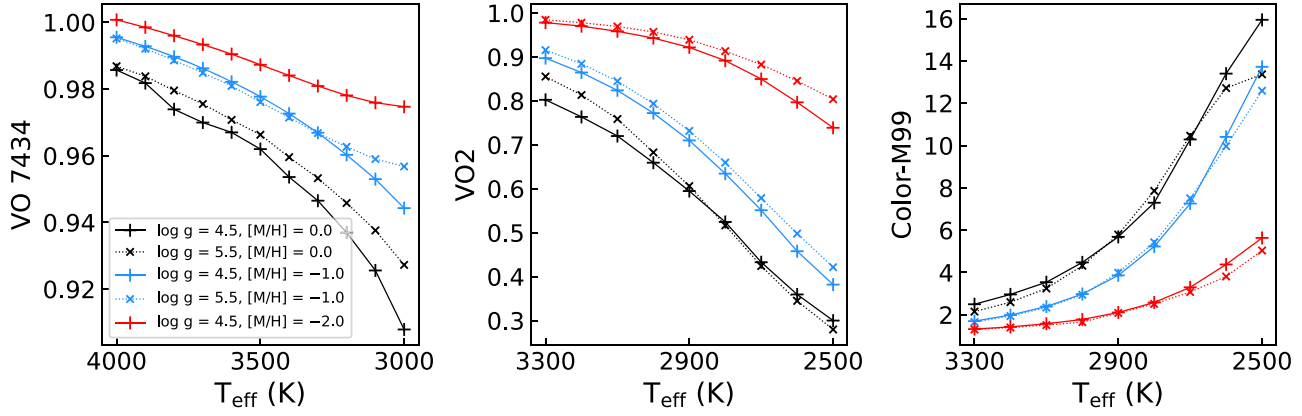


Figure 6. Models are plotted with the same colors as in the above figures.

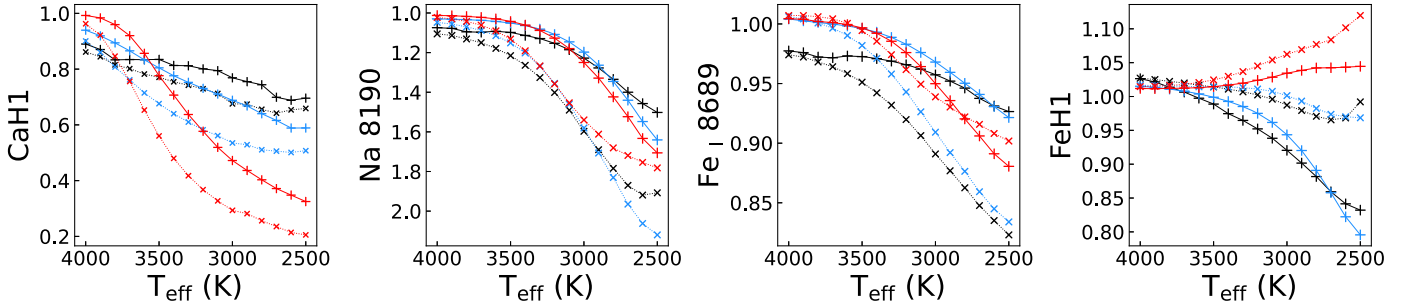


Figure 7. Indices that are highly sensitive to gravity and moderately sensitive to metallicity. Models are plotted with the same colors as in the above figures.

α -enrichment at the high- and low-temperature end, respectively. When the temperature drops to 3000 K and even lower, the indices $1.0 \mu\text{m}$, Cs-a, and $\text{CH}_4\text{-A}$ show the expected characteristics. These feature bands can be used to estimate $[M/H]$ after the temperature is determined.

After $[M/H]$ is determined, spectral features that are sensitive to $[\alpha/\text{Fe}]$ but still independent of gravity can be used to estimate α -abundance. Here we provide three indicators, VO 7434, VO2, and Color-M99, as shown in Figure 6. Indicator VO 7434 exhibits good sensitivity to metal abundance at the high-temperature end (3500–4000 K), while VO2 and Color-M99 could well complement its lack of availability due to its increasing sensitivity to gravity at the low-temperature end (2500–3500 K).

2.4. Spectral Features for the Determination of Gravity

As a final step, spectral features that are highly sensitive to gravity are preferred to determine $\log g$. The classical CaH band strengths measured by indices CaH1, CaH2, and CaH3 are dependent on both metallicity and surface gravity. With the metal abundance determined as a precondition, they could be great indicators of gravity.

In addition to the CaH bands, hydrides such as FeH and alkali lines such as the Na I and K I doublets are all very sensitive to gravity. We recommend the four indices shown in Figure 7, i.e., CaH1, Na 8190, FeH1, and Fe I 8689, because they have a high and regular sensitivity to gravity. Both Fe I 8689 and Na 8190 present a strong gravity dependence for both solar abundance and moderately metal-poor model sequences. The index FeH1 has a significant dependence on the three parameters that steadily becomes stronger toward lower temperatures. Most notably, the value of this index for the

models with $[M/H] = -2.0$ dex increases with decreasing temperature, while the index value for the solar abundance and moderately metal-poor models decreases. Besides, models with high gravity are less sensitive to temperature, except for the extremely metal-poor ones.

2.5. Parameter Estimation Steps

Accordingly, we can finally come up with a four-step solution to the problem due to the degeneracy effect on the parameter determination of M subdwarfs.

1. The temperature-sensitive pseudocontinuum colors such as PC4, PC5, Color-H02, C88-81, and C81-75 can be used to estimate the temperature for a subdwarf because these indices are hardly affected by the other atmospheric parameters. For the ultracool objects, infrared indices $\text{H}_2\text{O-B}$ and TLI-K are recommended for the dMs and sdMs, while $\text{H}_2\text{O-I}$ can be used for all metallicity subclasses as temperature indicators with slightly larger scatters.
2. Based on the determined temperature, the spectral index/colors Rb-b and PC6 can be used to estimate $[M/H]$ for subdwarfs with temperatures higher than 3000 K because they are not sensitive to either $[\alpha/\text{Fe}]$ or gravity within a given temperature scope. For subdwarfs with temperatures lower than 3000 K, the indices $1.0 \mu\text{m}$, Cs-a, and $\text{CH}_4\text{-A}$ could be useful.
3. The third free parameter, α -enhancement $[\alpha/\text{Fe}]$, can be estimated from VO 7434, VO2, and Color-M99, as shown in Figure 6, when T_{eff} and $[M/H]$ are known and fixed.
4. Finally, the spectral features that are particularly sensitive to surface gravity will be appropriate to determine $\log g$.

The multiple CaH bands (CaH1, CaH2, and CaH3) are useful as good indicators, combining with the features measured by indices Na 8190, Fe I 8689, and FeH1.

Particular attention needs to be paid to the fact that each index has its own suitable temperature range, and the results of these analyses are all based on low-resolution ($R \sim 2000$) synthetic spectra.

Besides, considering that the dynamic range of each index is different, and the reference wavelength regions are also affected differently by the observed factors, the applicable condition of each index is further discussed in the next section.

3. Effects of Different Spectral Quality and Resolution

The spectral indices were initially defined for low-resolution spectral research because low-resolution spectra are readily available and plentiful but lack the detailed structures observed at high resolutions that can be used to accurately infer atmospheric parameters (see, e.g., Rajpurohit et al. 2014).

In this section, we aim to investigate the effects of reduced spectral qualities that can be quantified by signal-to-noise ratios (S/Ns) and lower spectral resolutions.

3.1. Spectral Quality Variations

All of the model sequences in the T_{eff} -index diagrams above are based on the analysis results of the synthetic spectra without noise, but in the observations, the noise level of the flux directly affects the measurement accuracy of the index. Therefore, we add Gaussian noises corresponding to S/N = 200, 100, 50, 20, 10, and 5 to the synthetic spectra, calculate every index with the errors, and check the lowest S/N for which each index can still be used as a spectroscopic diagnostic.

As shown in Figure 8, in general, the pseudocontinuum colors are least affected by noise, and some (i.e., Color-H02, PC6, Color-M99) maintain some availability even when the S/N is as low as 5. On the contrary, a part of the diagnostics for metallicity and alpha abundance, i.e., Rb-b, Cs-a, CH₄-A, and VO 7434, depend very much on the quality of the spectrum; only when the S/N exceeds 100 do these indices finely distinguish between different abundances.

In addition, the effects from observation may introduce uncertainties and need to be calibrated carefully in advance, such as telluric line contamination, flux calibration issues, spectral reddening, and so on.

3.2. Lower Spectral Resolutions

At lower resolutions, problems could be raised by the information loss and the decreased number of sampling points involved in the index calculation.

As the resolution decreases, the overall shape of the spectral energy distribution remains basically unchanged, while the absorption lines become shallower and wider, the line wings change from sharp to flat, and some more structural characteristics such as the “jagged” TiO molecular band near 7000 Å gradually smooth until they are almost invisible at $R \sim 200$. Figure 9 shows a comparative example of a synthetic spectrum convolved to different resolutions.

On the other hand, the wavelength points within the reference bands of a spectral index decline in number with decreasing resolution. Assuming an observed spectrum is

sampled with a proper sampling rate, e.g., 2.5 times the FWHM of the line-spread function, some very narrow reference bands may not have any points left to calculate when the resolution drops to $R \sim 500$ or lower. In this situation, it is necessary to oversample the observed spectrum before calculating an index.

In order to investigate the changes in the spectral indices caused by different resolutions and explore the applicability of these features, we additionally convolve the synthetic spectra to $R \sim 1000, 500, \text{ and } 200$.

The indices that are mostly influenced by the resolution variation are expected to be the absorption atomic lines (such as the Na I doublet) and the narrowband molecular features (such as TiO5 and CaH2/3), which have one narrow reference band, as shown in the inset of Figure 9. It is important to recall that the spectral features explored in this study have been measured by the average or integrated flux within several specific bands.

Nevertheless, upon closer inspection, we find that the vast majority of the index trends of our recommended spectral features are resolution-independent down to $R \sim 200$, while they are also affected by noise levels very similarly as at resolution $R \sim 2000$. Since the performance of indices at these low resolutions is basically the same and does not provide significantly more information than Figure 8, we do not further illustrate the results here.

3.3. Discussion of Applicability to Observations

As a result, the exploration results of this paper can also be applied to very low resolution spectral data, such as the slitless spectroscopic survey conducted by the Chinese Space Station Telescope (CSST; Zhan 2011, 2021; Gong et al. 2019), which aims to deliver high-quality spectra covering 2500–10000 Å at $R \sim 200$ for hundreds of millions of stars and galaxies. Even so, it is worth noting that flux calibration with high precision and spectral quality are the foundation of the accuracy of index measurement. In many spectroscopic surveys, the flux calibration of cool stellar spectra often suffers larger uncertainty than the hot ones, mainly due to the lack of standard stars and inaccurate extinction correction.

We want to mention that the above-proposed technique to solve the long-standing issue due to the parameter degeneracy is still in its early stages, and more careful examinations are needed. In practice, a preset of initial values for the four parameters is required to start the fitting process. We suggest using the approach presented in Hejazi et al. (2022; Section 4.2 in their paper), which can allow us to develop an automated pipeline that will be applicable to future spectroscopic surveys.

In addition, a well-designed narrowband photometric survey covering the selected wavelength bands can also be a competitive implementation option. In recent years, many narrowband photometric surveys have been successfully carried out, such as the Javalambre Physics of the Accelerating Universe Astrophysical Survey (J-PAS; Marín-Franch et al. 2012; Benitez et al. 2014), the Javalambre-Photometric Local Universe Survey (J-PLUS; Cenarro et al. 2019; Yang et al. 2022; Wang et al. 2022), and the Southern Photometric Local Universe Survey (S-PLUS; Mendes de Oliveira et al. 2019; Almeida-Fernandes et al. 2022). Color-H02 (7350–7500 and 8900–9100 Å), for example, can be completely covered by filters 38 and 54 of J-PAS, which used 56 narrowband filters to sample the spectral energy distribution in the optical (3800–9200 Å) and achieved 1% photometric precision.

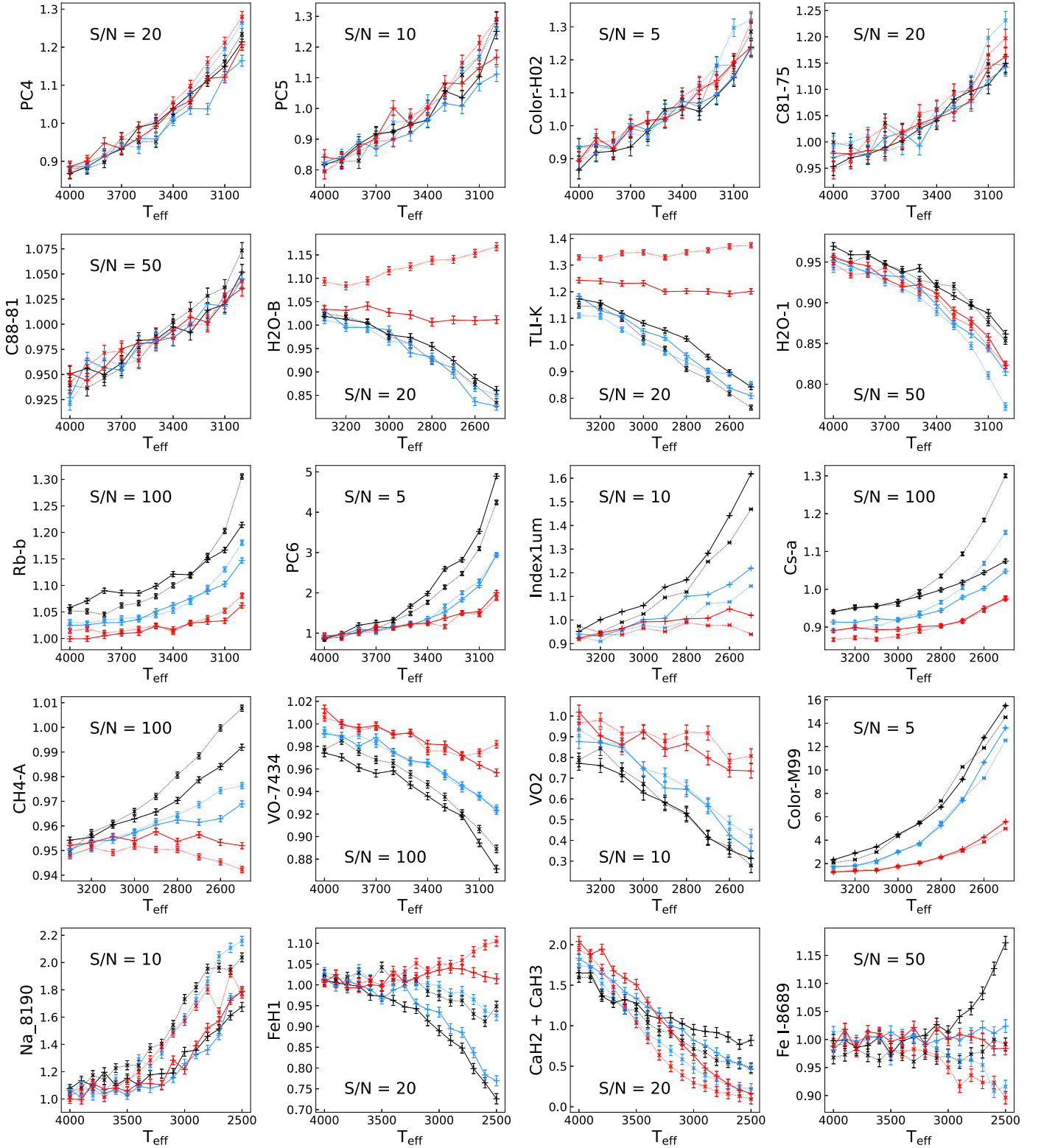


Figure 8. Recommended spectral indices derived from spectra with applicable lowest S/Ns. The models are plotted with the same colors as in the above figures. The error bars of each index representing 1σ errors are calculated from synthetic spectra with Gaussian noise added. The corresponding S/N is shown in each panel.

4. Summary and Conclusion

In this paper, we conduct an extended exploration of the parameter degeneracy of basic atmospheric parameters (T_{eff} , $\log g$, $[M/H]$, and $[\alpha/Fe]$) in the optical-to-NIR spectra of M subdwarfs. We assemble a large number of pseudocontinuum

colors and spectral indices that can quantify the slope of a given pseudocontinuum and band strength of molecular absorption, respectively. Based on the index trends of the latest PHOENIX BT-Settl model sequences, we illustrate with figures how the degenerated parameters affect the band strength of each spectral feature.

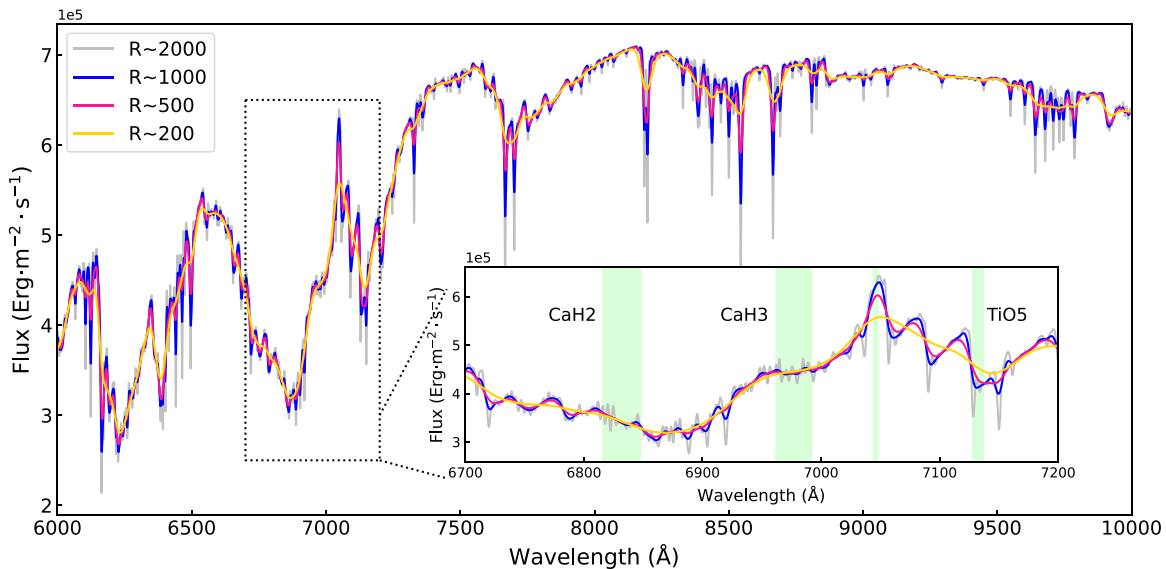


Figure 9. Synthetic spectrum ($T_{\text{eff}} = 3500$ K, $\log g = 5.0$, $[M/H] = -1.0$ dex, $[\alpha/Fe] = 0.4$ dex) at different resolutions: $R \sim 2000$, 1000, 500, and 200. The spectral region 6700–7200 Å is enlarged and shown in the inset. The CaH2, CaH3, and TiO5 feature bands and the reference band that they share are marked with light green shading.

Furthermore, we propose a four-step process (see Section 2.5) to sequentially determine T_{eff} , $[M/H]$, $[\alpha/Fe]$, and $\log g$, which extends the basic idea proposed by Jao et al. and effectively breaks the degeneracy. To this end, we suggest several spectral features to be used in each step that determines a specific parameter. Note that although the suggested features are characterized by indices for our quantified investigation, the practical way to use these features may include, but is not limited to, selecting corresponding wavelength regions for spectral fitting, calculating index values and obtaining empirical relationships, and adopting proper corresponding narrowband photometry instead of spectral data.

The effects of different spectral quality and resolution are also explored, drawing a conclusion that pseudocontinuum colors are least affected by noise among the recommended spectral features, while some diagnostics for metallicity and alpha abundance depend very much on the quality of the spectrum. Most of the index trends of the spectral features that we recommend are resolution-independent down to $R \sim 200$, but they are also affected by noise levels very similarly as at high resolution. Finally, we discuss the possibility of using

narrowband photometry as an alternative option for spectral data.

We thank the anonymous referee for helpful comments and suggestions that significantly improved our manuscript. Z.S. thanks Dr. Fu X.T. for the thoughtful discussion. This work was funded by the National Key R&D Program of China (No. 2019YFA0405500), the National Natural Science Foundation of China (NSFC grant Nos. 11973001, 12090040, 12090044, and 12103068), and Science Research Grants from the China Manned Space Project Nos. CMS-CSST-2021-B05 and CMS-CSST-2021-A08.

Appendix

Pseudocontinuum Colors and Spectral Indices with Their Reference Bands

In Sections 2.2 to 2.4, we explore parameter degeneracy via spectral indices of model sequences. For reference, the corresponding definition of pseudocontinuum colors and spectral features from the literature are listed in Tables A1 and A2, respectively.

Table A1
The Pseudocontinuum Colors

| Pseudocontinuum Color | Name in This Paper | Numerator (Å) | Denominator (Å) | Source |
|-----------------------|--------------------|---------------|-----------------|---------------------------|
| BlueColor | | 6100–6300 | 4500–4700 | Covey et al. (2007) |
| Color6545 | | 6545–6549 | 7560–7564 | Yi et al. 2014 |
| Color-M | | 8105–8155 | 6510–6560 | Lépine et al. (2003) |
| Color-1 | Color-H02 | 8900–9100 | 7350–7500 | Hawley et al. (2002) |
| Color-1 | Color-C07 | 8900–9100 | 7350–7550 | Covey et al. (2007) |
| Color-a | | 9800–9850 | 7300–7350 | Kirkpatrick et al. (1999) |
| Color-b | | 9800–9850 | 7000–7050 | Kirkpatrick et al. (1999) |
| Color-c | | 9800–9850 | 8100–8150 | Kirkpatrick et al. (1999) |
| Color-d | | 9675–9875 | 7350–7550 | Kirkpatrick et al. (1999) |
| PC1 | | 7030–7050 | 6525–6550 | Martin et al. (1996) |
| PC2 | | 7540–7580 | 7030–7050 | Martin et al. (1996) |
| PC3 | | 8235–8265 | 7540–7580 | Martin et al. (1996) |
| PC3 | PC3-M99 | 8230–8270 | 7540–7580 | Martin et al. (1999) |
| PC4 | | 9190–9225 | 7540–7580 | Martin et al. (1996) |
| PC5 | | 9800–9880 | 7540–7580 | Martin et al. (1996) |
| PC6 | | 9090–9130 | 6500–6540 | Martin et al. (1999) |

Note. Pseudocontinuum colors assembled from the literature. Some of the colors are renamed to avoid the problem of duplicate names.

Table A2
The Spectral Features Defined in the Literature

| Spectral Index | Name in This Paper | Numerator (Å) | Denominator (Å) | Method | Source |
|----------------------|------------------------------|---------------|----------------------|------------|------------------------------|
| CaOH | | 6230–6240 | 6345–6354 | Average | Reid et al. (1995) |
| CaH1 | | 6380–6390 | 6345–6355, 6410–6420 | Average | Reid et al. (1995) |
| CaH2 | | 6814–6846 | 7042–7046 | Average | Reid et al. (1995) |
| CaH3 | | 6960–6990 | 7042–7046 | Average | Reid et al. (1995) |
| TiO2 | | 7058–7061 | 7043–7046 | Average | Reid et al. (1995) |
| TiO3 | | 7092–7097 | 7079–7084 | Average | Reid et al. (1995) |
| TiO4 | | 7130–7135 | 7115–7120 | Average | Reid et al. (1995) |
| TiO5 | | 7126–7135 | 7042–7046 | Average | Reid et al. (1995) |
| VO 7434 | | 7430–7470 | 7550–7570 | Average | Hawley et al. (2002) |
| VO2 | | 7920–7960 | 8130–8150 | Average | Lépine et al. (2003) |
| Rb-b | 7922.6–7932.6, 7962.6–7972.6 | | 7942.6–7952.6 | Average | Kirkpatrick et al. (1999) |
| Na 8190 | | 8140–8165 | 8173–8210 | Average | Hawley et al. (2002) |
| Fe ₁ 8689 | | 8684–8694 | 8664–8674 | Average | Covey et al. (2007) |
| Cs-a | 8496.1–8506.1, 8536.1–8546.1 | | 8516.1–8526.1 | Average | Kirkpatrick et al. (1999) |
| FeH1 | | 8560–8660 | 8685–8725 | Average | Martin et al. (1999) |
| 1.0 μm | | 10400–10500 | 8750–8850 | Integrated | Geballe et al. (2002) |
| CH ₄ -A | | 12950–13250 | 12500–12800 | Average | Burgasser et al. (2002) |
| H ₂ O-1 | | 13350–13450 | 12950–13050 | Average | Slesnick et al. (2004) |
| H ₂ O-B | | 15050–15250 | 15750–15950 | Average | Burgasser et al. (2002) |
| TLI-K | | 19700–19900 | 22200–22400 | Average | Almendros-Abad et al. (2022) |

Note. Spectral indices assembled from the literature and recommended in the four-step process. For each index, one can use the corresponding method to calculate the flux over the numerator and denominator wavelength ranges and derive the index value according to Equation (2). In the case of CaH1, Rb-b, and Cs-a, two bands in the Numerator/Denominator columns are both used as the feature/pseudocontinuum.

ORCID iDs

Shuo Zhang (张硕)  <https://orcid.org/0000-0003-1454-1636>
Hua-Wei Zhang (张华伟)  <https://orcid.org/0000-0002-7727-1699>
Derek Homeier  <https://orcid.org/0000-0002-8546-9128>
Rui Wang (王瑞)  <https://orcid.org/0000-0001-6767-2395>
Neda Hejazi  <https://orcid.org/0000-0001-5541-6087>
Yin-Bi Li (李荫碧)  <https://orcid.org/0000-0001-7607-2666>
A-Li Luo (罗阿理)  <https://orcid.org/0000-0001-7865-2648>

References

- Allard, F. 1990, PhD thesis, Centre de Recherche Astrophysique de Lyon
Allard, F., Hauschildt, P. H., Alexander, D. R., Tamanai, A., & Schweitzer, A. 2001, *ApJ*, **556**, 357
Allard, F., Homeier, D., & Freytag, B. 2012, *RSPITA*, **370**, 2765
Allard, F., Homeier, D., & Freytag, B. 2014, in ASI Conf. Ser. 11, International Workshop on Stellar Spectral Libraries, ed. H. P. Singh, P. Prugniel, & I. Vauglin (Astronomical Society of India), 33
Allard, F., Homeier, D., Freytag, B., Schaffnerberger, W., & Rajpurohit, A. S. 2013, *MSAIS*, **24**, 128
Allers, K. N., Jaffe, D. T., Luhman, K. L., et al. 2007, *ApJ*, **657**, 511
Allers, K. N., & Liu, M. C. 2013, *ApJ*, **772**, 79

- Almeida-Fernandes, F., SamPedro, L., Herpich, F. R., et al. 2022, *MNRAS*, **511**, 4590
- Almendros-Abad, V., Mužić, K., Moitinho, A., Krone-Martins, A., & Kubiak, K. 2022, *A&A*, **657**, A129
- Baraffé, I., Homeier, D., Allard, F., & Chabrier, G. 2015, *A&A*, **577**, A42
- Benedict, G. F., Henry, T. J., Franz, O. G., et al. 2016, *AJ*, **152**, 141
- Benitez, N., Dupke, R., Moles, M., et al. 2014, arXiv:1403.5237
- Bochanski, J. J., Hawley, S. L., Covey, K. R., et al. 2010, *AJ*, **139**, 2679
- Bochanski, J. J., Savcheva, A., West, A. A., & Hawley, S. L. 2013, *AJ*, **145**, 40
- Bonfils, X., Delfosse, X., Udry, S., et al. 2005, *A&A*, **442**, 635
- Buder, S., Sharma, S., Kos, J., et al. 2021, *MNRAS*, **506**, 150
- Burgasser, A. J., Cruz, K. L., Cushing, M., et al. 2010, *ApJ*, **710**, 1142
- Burgasser, A. J., Geballe, T. R., Leggett, S. K., Kirkpatrick, J. D., & Golimowski, D. A. 2006, *ApJ*, **637**, 1067
- Burgasser, A. J., Kirkpatrick, J. D., Brown, M. E., et al. 2002, *ApJ*, **564**, 421
- Cenarro, A. J., Moles, M., Cristóbal-Hornillos, D., et al. 2019, *A&A*, **622**, A176
- Chabrier, G. 2003, *PASP*, **115**, 763
- Conroy, C., & van Dokkum, P. 2012, *ApJ*, **747**, 69
- Covey, K. R., Lada, C. J., Román-Zúñiga, C., et al. 2010, *ApJ*, **722**, 971
- Covey, K. R., Ivezić, Ž., Schlegel, D., et al. 2007, *AJ*, **134**, 2398
- Cushing, M. C., Rayner, J. T., & Vacca, W. D. 2005, *ApJ*, **623**, 1115
- Cushing, M. C., Tokunaga, A. T., & Kobayashi, N. 2000, *AJ*, **119**, 3019
- Delfosse, X., Forveille, T., Ségransan, D., et al. 2000, *A&A*, **364**, 217
- Dieterich, S. B., Simler, A., Henry, T. J., & Jao, W.-C. 2021, *AJ*, **161**, 172
- Dressing, C. D., & Charbonneau, D. 2013, *ApJ*, **767**, 95
- Du, B., Luo, A. L., Zhang, S., et al. 2021, *RAA*, **21**, 202
- Dupuy, T. J., & Liu, M. C. 2017, *ApJS*, **231**, 15
- Freytag, B., Allard, F., Ludwig, H. G., Homeier, D., & Steffen, M. 2010, *A&A*, **513**, A19
- Freytag, B., Steffen, M., Ludwig, H. G., et al. 2012, *JCoPh*, **231**, 919
- Gaidos, E., & Mann, A. W. 2014, *ApJ*, **791**, 54
- Geballe, T. R., Knapp, G. R., Leggett, S. K., et al. 2002, *ApJ*, **564**, 466
- Gizis, J. E. 1997, *AJ*, **113**, 806
- Gong, Y., Liu, X., Cao, Y., et al. 2019, *ApJ*, **883**, 203
- Gustafsson, B., Edvardsson, B., Eriksson, K., et al. 2008, *A&A*, **486**, 951
- Hamilton, D., & Stauffer, J. R. 1993, *AJ*, **105**, 1855
- Hauschildt, P. H., Baron, E., & Allard, F. 1997, *ApJ*, **483**, 390
- Hawley, S. L., Covey, K. R., Knapp, G. R., et al. 2002, *AJ*, **123**, 3409
- Hayden, M. R., Bovy, J., Holtzman, J. A., et al. 2015, *ApJ*, **808**, 132
- Hejazi, N., Lépine, S., Homeier, D., Rich, R. M., & Shara, M. M. 2020, *AJ*, **159**, 30
- Hejazi, N., Lépine, S., & Nordlander, T. 2022, *ApJ*, **927**, 122
- Henry, T. J., Jao, W.-C., Subasavage, J. P., et al. 2006, *AJ*, **132**, 2360
- Jao, W.-C., Henry, T. J., Beaulieu, T. D., & Subasavage, J. P. 2008, *AJ*, **136**, 840
- Kesseli, A. Y., Kirkpatrick, J. D., Fajardo-Acosta, S. B., et al. 2019, *AJ*, **157**, 63
- Kirkpatrick, J. D., Henry, T. J., & McCarthy, D. W. J. 1991, *ApJS*, **77**, 417
- Kirkpatrick, J. D., Henry, T. J., & Simons, D. A. 1995, *AJ*, **109**, 797
- Kirkpatrick, J. D., Reid, I. N., Liebert, J., et al. 1999, *ApJ*, **519**, 802
- Lépine, S., Rich, R. M., & Shara, M. M. 2003, *AJ*, **125**, 1598
- Lépine, S., Rich, R. M., & Shara, M. M. 2007, *ApJ*, **669**, 1235
- Lodieu, N., Allard, F., Rodrigo, C., et al. 2019, *A&A*, **628**, A61
- Majewski, S. R., Schiavon, R. P., Frinchaboy, P. M., et al. 2010, *AJ*, **154**, 94
- Mann, A. W., Brewer, J. M., Gaidos, E., Lépine, S., & Hilton, E. J. 2013a, *AJ*, **145**, 52
- Mann, A. W., Dupuy, T., Kraus, A. L., et al. 2019, *ApJ*, **871**, 63
- Mann, A. W., Feiden, G. A., Gaidos, E., Boyajian, T., & von Braun, K. 2015, *ApJ*, **804**, 64
- Mann, A. W., Gaidos, E., & Ansdell, M. 2013b, *ApJ*, **779**, 188
- Marín-Franch, A., Chueca, S., Moles, M., et al. 2012, *Proc. SPIE*, **8450**, 84503S
- Martín, E. L., Delfosse, X., Basri, G., et al. 1999, *AJ*, **118**, 2466
- Martin, E. L., Rebolo, R., & Zapatero-Osorio, M. R. 1996, *ApJ*, **469**, 706
- McConnell, N. J., Lu, J. R., & Mann, A. W. 2016, *ApJ*, **821**, 39
- McLean, I. S., McGovern, M. R., Burgasser, A. J., et al. 2003, *ApJ*, **596**, 561
- McLean, I. S., Wilcox, M. K., Becklin, E. E., et al. 2000, *ApJL*, **533**, L45
- Mendes de Oliveira, C., Ribeiro, T., Schoenell, W., et al. 2019, *MNRAS*, **489**, 241
- Mould, J. R. 1976a, *ApJ*, **210**, 402
- Mould, J. R. 1976b, *A&A*, **48**, 443
- Muirhead, P. S., Mann, A. W., Vanderburg, A., et al. 2015, *ApJ*, **801**, 18
- Neves, V., Bonfils, X., Santos, N. C., et al. 2012, *A&A*, **538**, A25
- Passegger, V. M., Reiners, A., Jeffers, S. V., et al. 2018, *A&A*, **615**, A6
- Passegger, V. M., Wende-von Berg, S., & Reiners, A. 2016, *A&A*, **587**, A19
- Rains, A. D., Žerjal, M., Ireland, M. J., et al. 2021, *MNRAS*, **504**, 5788
- Rajpurohit, A. S., Allard, F., Rajpurohit, S., et al. 2018a, *A&A*, **620**, A180
- Rajpurohit, A. S., Allard, F., Teixeira, G. D. C., et al. 2018b, *A&A*, **610**, A19
- Rajpurohit, A. S., Reylé, C., Allard, F., et al. 2013, *A&A*, **556**, A15
- Rajpurohit, A. S., Reylé, C., Allard, F., et al. 2014, *A&A*, **564**, A90
- Rajpurohit, A. S., Reylé, C., Allard, F., et al. 2016, *A&A*, **596**, A33
- Reid, I. N., Burgasser, A. J., Cruz, K. L., Kirkpatrick, J. D., & Gizis, J. E. 2001, *AJ*, **121**, 1710
- Reid, I. N., & Gizis, J. E. 1997, *AJ*, **114**, 1992
- Reid, I. N., Hawley, S. L., & Gizis, J. E. 1995, *AJ*, **110**, 1838
- Reylé, C., Jardine, K., Fouqué, P., et al. 2021, *A&A*, **650**, A201
- Rojas-Ayala, B., Covey, K. R., Muirhead, P. S., & Lloyd, J. P. 2012, *ApJ*, **748**, 93
- Scholz, A., Muzic, K., Geers, V., et al. 2012, *ApJ*, **744**, 6
- Slesnick, C. L., Hillenbrand, L. A., & Carpenter, J. M. 2004, *ApJ*, **610**, 1045
- Spiniello, C., Barnabè, M., Koopmans, L. V. E., & Trager, S. C. 2015, *MNRAS*, **452**, L21
- Testi, L., D'Antona, F., Ghinassi, F., et al. 2001, *ApJL*, **552**, L147
- Tokunaga, A. T., & Kobayashi, N. 1999, *AJ*, **117**, 1010
- Valenti, J. A., Piskunov, N., & Johns-Krull, C. M. 1998, *ApJ*, **498**, 851
- Veyette, M. J., Muirhead, P. S., Mann, A. W., et al. 2017, *ApJ*, **851**, 26
- Wang, C., Bai, Y., Yuan, H., et al. 2022, *A&A*, **664**, A38
- Weights, D. J., Lucas, P. W., Roche, P. F., Pinfield, D. J., & Riddick, F. 2009, *MNRAS*, **392**, 817
- Winters, J. G., Henry, T. J., Lurie, J. C., et al. 2015, *AJ*, **149**, 5
- Woolf, V. M., Lépine, S., & Wallerstein, G. 2009, *PASP*, **121**, 117
- Yang, L., Yuan, H., Xiang, M., et al. 2022, *A&A*, **659**, A181
- Yi, Z., Luo, A., Song, Y., et al. 2014, *AJ*, **147**, 33
- Zhan, H. 2011, *SSPMA*, **41**, 1441
- Zhan, H. 2021, *Chin. Sci. Bull.*, **66**, 1290
- Zhang, S., Luo, A. L., Comte, G., et al. 2021, *ApJ*, **908**, 131
- Zhang, Z. 2019, *MNRAS*, **489**, 1423
- Zhang, Z., Liu, M. C., Best, W. M. J., et al. 2018, *ApJ*, **858**, 41
- Zhang, Z. H., Homeier, D., Pinfield, D. J., et al. 2017a, *MNRAS*, **468**, 261
- Zhang, Z. H., Pinfield, D. J., Gálvez-Ortiz, M. C., et al. 2017b, *MNRAS*, **464**, 3040